Mon. Not. R. Astron. Soc. **000**, 000–000 (0000) Printed 1 February 2008 (MN LATEX style file v2.2)

arXiv:0707.0469v2 [astro-ph] 24 Jul 2007

WMAP 3yr data with the CCA: anomalous emission and impact of component separation on the CMB power spectrum

A. Bonaldi, S. Ricciardi, S. Leach, F. Stivoli, C. Baccigalupi, G. De Zotti

1 February 2008

ABSTRACT

The Correlated Component Analysis (CCA) allows us to estimate how the different diffuse emissions mix in CMB experiments, taking also into account complementary information from other surveys. It is especially useful to deal with possible additional components for which little or no prior information exists. An application of CCA to WMAP maps assuming that only the canonical Galactic emissions (synchrotron, free-free, and thermal dust) are present, highlights the widespread presence of a spectrally flat "synchrotron" component, largely uncorrelated with the synchrotron template, suggesting that an additional foreground is indeed required. We have tested various spectral shapes for such component, namely a power law as expected if it is flat synchrotron, and two spectral shapes that may fit the spinning dust emission: a parabola in the $\log S$–$\log \nu$ plane, and a grey body. If the spatial distribution of the additional ("anomalous") component is not constrained a priori it is found to be always tightly correlated with thermal dust, but the correlation is not perfect. Quality tests applied to the reconstructed CMB maps clearly disfavour two of the models. The CMB power spectra, estimated from CMB maps reconstructed exploiting the three surviving foreground models, are generally consistent with the WMAP ones, although at least one of them gives a significantly higher quadrupole moment than found by the WMAP team. Taking foreground modeling uncertainties into account, we find that the mean quadrupole amplitude for the three "good" models is less than 1σ below the expectation from the standard ΛCDM model. Also the other reported deviations from model predictions are found not to be statistically significant, except for the excess power at $l \simeq 40$. We confirm the evidence for a marked north south asymmetry in the large scale ($l < 20$) CMB anisotropies, which is stable with respect to the foreground parametrization we adopted. We also present a first, albeit preliminary, all sky map of the "anomalous emission".

1 INTRODUCTION

The *Wilkinson Microwave Anisotropy Probe* (WMAP, Bennett et al. 2003; Spergel et al. 2006) data are having a dominant role in determining the reference cosmological model. It is therefore important to get an in depth understanding of all the uncertainties in the data analysis and of their effects on the estimates of the angular power spectrum of the Cosmic Microwave Background (CMB), from which the values of the fundamental cosmological parameters are derived.

In this paper we present a new investigation, exploiting a novel technique, of the effect of foreground contamination. CMB power spectrum analyses are normally done removing a substantial fraction of the sky ($\simeq 25\%$) around the Galactic plane where Galactic emissions are stronger. However, the uncertainties in the underlying foreground emission make it possible that a relevant contribution from them remains, even when large sky cuts are considered. Slosar & Seljak (2004) developed a formalism to incorporate foreground uncertainties and the effect of sky cuts in the estimates of errors on multipole moments. Slosar et al. (2004) marginalized over the foreground templates produced by Bennett et al. (2003) from WMAP data. O'Dwyer (2005) and O'Dwyer et al. (2004) have shown that it is possible to include the foreground components in a self-consistent fashion within the statistical framework of their approach to power spectrum estimation, based on a Bayesian statistical analysis of the data utilizing Gibbs Sampling.

Here we deal with foregrounds applying to the three-year WMAP data the Correlated Component Analysis (CCA, Bedini et al. 2005; Bonaldi et al. 2006), which exploits a second order statistics of the data to estimate the spectral behaviour of the mixed components directly from the WMAP data. The method also allows us to incorporate the additional information from other surveys, such as the Haslam et al. (1982) 408 MHz map, the IRAS/COBE dust emission map (Finkbeiner et al. 1999), and the extinction corrected Hα map (Dickinson et al. 2003), as a tracer of free-free emission. At variance with most alternative techniques, CCA allows us to perform an essentially all-sky component separation: only a narrow strip around the Galactic equator ($|b| < 3^\circ$, $\simeq 5\%$ of the sky) needs to be removed (Bonaldi et al. 2006).

Of course, we need to specify a priori which foreground components are contributing to the maps and describe their frequency spectra with a small number of parameters, as specified is § 2, and this brings in the issue of the possible presence of one more Galactic component, in addition to the well established synchrotron, free-free, and thermal dust emissions. In § 3 we describe the estimation with CCA of the mixing matrix, exploited to reconstruct the maps of astrophysical components using an inversion algorithm that, in our case, is the harmonic Wiener Filter, as described in § 4. The properties of the reconstructed foreground components are discussed in § 5, and those of the CMB in § 6 where we analyze the uncertainties on the derived CMB power spectrum ensuing from those on foreground properties, especially in relation to the reported deviations from predictions of the "concordance" cosmological model (Spergel et al. 2006). The main conclusions are summarized in § 7.

2 DIFFUSE COMPONENTS IN THE WMAP BANDS

We summarize here the frequency spectra of diffuse components, in terms of antenna temperature. The CMB blackbody spectrum is:

$$T_{\rm A,CMB}(\nu) = \frac{(h\nu/kT_{\rm CMB})^2 \exp(h\nu/kT_{\rm CMB})}{(\exp(h\nu/kT_{\rm CMB})-1)^2} \qquad (1)$$

where h and k are the Planck and the Boltzmann constant, respectively, and $T_{\rm CMB} = 2.726\,{\rm K}$.

The free-free emission spectrum is also quite uniform and well approximated, in the frequency range of interest, by:

$$T_{\rm A,ff}(\nu) \propto \nu^{-2.14} \qquad (2)$$

It is difficult to obtain a spatial template of this emission since synchrotron dominates radio surveys and thermal dust dominates far-IR surveys. A good tracer of free-free emission are $H\alpha$ maps, but they need to be corrected for dust extinction, and this correction adds a significant uncertainty (Dickinson et al. 2003).

The synchrotron spectrum is usually modeled as:

$$T_{\rm A,synch}(\nu) \propto \nu^{-\beta_s}. \qquad (3)$$

Its spectral index, β_s, is known to vary across the sky, reflecting the variations of the energy index of relativistic electrons (Rybicki & Lightman 1979). The WMAP team (Bennett et al. 2003; Hinshaw et al. 2006) find steeper values ($\beta_s \simeq 3$) at high Galactic latitudes and flatter values ($\beta_s \simeq 2.5$) close to star-forming regions, especially in the Galactic plane. The mean value is 2.65 between 408 MHz and the K-band, and 2.69 between 408 MHz and the Q-band. A spectral steepening is expected at high microwave frequencies, as a consequence of electron ageing effects (Banday & Wolfendale 1991). The Haslam et al. (1982) 408 MHz map is commonly used as a synchrotron template.

The spectrum of the thermal (vibrational) emission from dust grains in the interstellar medium is conveniently described by a grey body:

$$T_{\rm A,dust}(\nu) \propto \frac{\nu^{\beta_d+1}}{\exp(h\nu/kT_{\rm dust})-1} \qquad (4)$$

with $T_{\rm dust} \sim 18\,{\rm K}$ and $\beta_d \sim 1.67$ at mm wavelengths (Finkbeiner et al. 1999). Both $T_{\rm dust}$ and β_d are expected to vary across the sky due to variations of the interstellar radiation field and of the dust grains composition. Measurements of β_d generally lie in the range $1.5 \leqslant \beta_d \leqslant 2.0$, but an even broader range has been observed by the PRONAOS experiment (Dupac et al. 2003): $0.8 \leqslant \beta_d \leqslant 2.4$. The WMAP data only weakly constrain the dust spectral index (Hinshaw et al. 2006). The most frequently used spatial template of thermal dust emission is the one worked out by Finkbeiner et al. (1999) combining IRAS and COBE maps.

In recent years evidence has been reported for an additional, thermal dust correlated component called "anomalous microwave emission", that may dominate, at least in some Galactic regions, in the 20–40 GHz range, where it has a spectrum similar to synchrotron. It may be originated by tiny, fast spinning, dust grains (Draine & Lazarian 1998; de Oliveira-Costa et al. 1999, 2002). Indications of this emission were found by analyses of CMB experiments like Saskatoon (de Oliveira-Costa et al. 1997), 19 GHz (de Oliveira-Costa et al. 1998), Tenerife (de Oliveira-Costa et al. 1999, 2002; Mukherjee et al. 2001); Python V (Mukherjee et al. 2003). Although Bennett et al. (2003) concluded that spinning dust emission contributes less than 5% of the WMAP Ka-band antenna temperature, evidence of the anomalous emission were uncovered combining WMAP data with other measurements, especially at lower frequencies (Lagache 2003; de Oliveira-Costa et al. 2004; Finkbeiner 2004; Watson et al. 2005; Davies et al. 2006). Moreover, the polarization properties of the dust-correlated low-frequency component differ from those of the component well correlated with the Haslam template, suggesting a different emission mechanism (Page et al. 2006). Nevertheless, the exact nature, the spectral properties, and the spatial distribution of this foreground remain uncertain. There is not general agreement even on its existence; a combination of free-free emission and of strongly self absorbed synchrotron could also account for the data (Hinshaw et al. 2006).

Table 1. WMAP channels

Channel	K	Ka	Q	V	W
Frequency (GHz)	23	33	41	61	94
Resolution (degrees)	0.93	0.68	0.53	0.35	<0.23
σ_0(mK)	1.42	1.45	2.21	3.11	6.50
mean pixel rms (mK)	0.07	0.07	0.07	0.09	0.1

Point sources are another important foreground component, but their contribution to the power spectrum is important only on scales $\lesssim 1^\circ$, while in this analysis we are mostly interested on larger scales, where diffuse emissions dominate. For the present analysis we will simply need to mask the brightest sources, as described in the following sections.

3 MIXING MATRIX ESTIMATION WITH CCA

3.1 Outline of the method

As usual, we express the data vector $\mathbf{x}$ in each pixel as:

$$\mathbf{x} = \mathbf{H}\mathbf{s} + \mathbf{n} \qquad (5)$$

where $\mathbf{H}$ is a $M \times N$ mixing matrix, $\mathbf{s}$ is the N-vector of sources (components) and $\mathbf{n}$ the M-vector of instrumental noise (M is then the number of independent maps used in the analysis). The generic element $h_{\rm dc}$ of the mixing matrix is proportional to the spectrum of the c-th source at an effective frequency within the d-th sensor passband. Using eq. (5) we implicitly assume that the spatial pattern of the physical processes is independent of frequency and that the effects of the telescope beam has been equalized in all channels.

Given a generic signal $\mathbf{X}$, defined in a two dimensional space with coordinates (ξ, η), the covariance matrix of this signal is:

$$\mathbf{C}_X(\tau,\psi) = \langle [\mathbf{X}(\tau,\psi) - \mu][\mathbf{X}(\xi+\tau,\eta+\psi) - \mu]^T \rangle \qquad (6)$$

where $\langle ... \rangle$ denotes expectation under the appropriate joint probability, μ is the mean vector and the superscript T means transposition. Every covariance matrix is characterized by the shift pair (τ, ψ), where τ and ψ are increments in the ξ and η coordinates.

From eq. (5) we can easily derive a relation between the data covariance matrix $\mathbf{C}_x$ at a certain lag, the source covariance matrix $\mathbf{C}_s$ at the same lag, the mixing matrix $\mathbf{H}$, and the noise covariance matrix $\mathbf{C}_n$:

$$\mathbf{C}_x(\tau,\psi) = \mathbf{H}\mathbf{C}_s(\tau,\psi)\mathbf{H}^T + \mathbf{C}_n(\tau,\psi). \tag{7}$$

The covariance matrix $\mathbf{C}_x$ can be estimated from the data as:

$$\hat{\mathbf{C}}_x(\tau,\psi) = \frac{1}{N_p}\sum_{\xi,\eta}[\mathbf{x}(\xi,\eta)-\mu_x][\mathbf{x}(\xi+\tau,\eta+\phi)-\mu_x]^T \tag{8}$$

where N_p is the number of pixels sampling the data. Given a noise process, we can model the noise correlation matrix $\mathbf{C}_n$: for example, if noise can be assumed signal-independent, white and zero-mean, for $(\tau,\psi) = (0,0)$ $\mathbf{C}_n$ is a diagonal matrix whose elements are the noise variances in the measured channels, while for $(\tau,\psi) \neq (0,0)$ $\mathbf{C}_n$ is the null $M \times M$ matrix. If the noise process deviates significantly from this ideal model, $\mathbf{C}_n$ can be computed using Monte Carlo on noise maps in the same way we did for $\mathbf{C}_x$.

Once $\mathbf{C}_x$ and $\mathbf{C}_n$ are known, eq. (7) can be used to identify the mixing operator $\mathbf{H}$. The strategy of CCA is to parameterize the mixing matrix to reduce the number of unknowns and to take into account enough nonzero shift pairs (τ,ψ) to estimate both $\mathbf{H}$ and $\mathbf{C}_s$. To solve the identification problem we perform the minimization:

$$(\Gamma(:,:)) = \text{argmin}\sum_{\tau,\psi} \parallel \mathbf{H}(\Gamma)\mathbf{C}_s[\Sigma(\tau,\psi)]\mathbf{H}^T(\Gamma) + \tag{9}$$

$$-\hat{\mathbf{C}}_x(\tau,\psi) - \mathbf{C}_n(\tau,\psi) \parallel$$

where Γ is the vector of all parameters defining $\mathbf{H}$ and $\Sigma(:,:)$ is the vector containing all the unknown elements of matrices $\mathbf{C}_s$ for every shift pair.

The main product of CCA is an estimate of the mixing matrix $\mathbf{H}$. The result is defined apart from the normalization of the different signals at a given frequency. Therefore we estimate a normalized mixing matrix, obtained by assigning value 1 to all the elements of an arbitrarily chosen row. This matrix can be used to perform the source reconstruction with standard inversion methods. In our case, this is done by harmonic Wiener Filtering, as we will describe in § 4.

3.2 Input data

The basic data are the three-year WMAP maps in the K, Ka, Q, V and W bands, whose main characteristics are summarized in Table 1. The values of σ_0 reported for every channel allow us to calculate a noise map at each frequency as $\sigma = \sigma_0 N_{\rm obs}^{-1/2}$, where $N_{\rm obs}$ is the map of the effective number of observations, provided with the data. The mean rms per pixel relative to each channel at full resolution is also reported.

The maps were then smoothed to the common resolution of 1° (Bennett et al. 2003). Since we do not have an exact formula to associate an rms level to each map after smoothing, we therefore simulated a set of ten WMAP noise maps at each WMAP frequency using the corresponding σ_0 and $N_{\rm obs}$. We then smoothed them to the 1° resolution, and computed the mean rms for each channel.

We assumed the noise process to be gaussian with variance equal to the mean of the all-sky variances of the simulated noise maps. Then $\mathbf{C}_n(\tau,\psi)$ is a diagonal matrix whose elements are these empirical variances for $(\tau,\psi) = (0,0)$, and the null matrix for $(\tau,\psi) \neq (0,0)$. In eq. (7) we then treat $\mathbf{C}_n(\tau,\psi)$ as a diagonal matrix whose elements are these empirical variances for $(\tau,\psi) = (0,0)$, and as null matrices for $(\tau,\psi) \neq (0,0)$.

Strong point sources can contribute substantially to the mean surface brightness in some pixels and, since their frequency spectra are generally different from those of diffuse components, they may bias the mixing matrix estimates. Source fluxes are highly diluted in the relatively low resolution maps used here and we find that the point source effects become negligible once we mask a region of 1° radius around each source contained in the three-year point source catalogue provided with the WMAP data. In addition, based on the analysis by Bonaldi et al. (2006), we applied a Galactic cut of ±3°. Finally, we masked few highly contaminated regions, namely CenA, the Large Magellanic Cloud, ρ Oph, Orion A, Orion B and Tau A.

To get a better leverage for foreground differentiation we complemented the WMAP data with a “thermal dust” and a “synchrotron” map. The former was obtained extrapolating to 850 GHz the dust map by Schlegel et al. (1998) using the best fit model of Finkbeiner et al. (1999). The latter is based on the Haslam et al. (1982) a 408 MHz map. Even if the Haslam map is often assumed to be pure synchrotron, contributions from the free-free emission can be important, especially on the Galactic plane (Paladini et al. 2005). Our “synchrotron” map was then obtained by subtracting from the Haslam map the free-free contribution estimated from the $H\alpha$ map corrected for dust absorption (Dickinson et al. 2003).

3.3 Analysis

To reduce the number of unknowns to a manageable level we need to parameterize the mixing matrix $\mathbf{H}$. This means we have to exploit our knowledge of foregrounds to model the WMAP data in terms of a small number of parameters. On the other hand, as mentioned in § 1, we are not even sure about the number of foreground components that need to be taken into account.

Also, foreground spectral parameters vary across the sky. Therefore we would ideally want a map of the values of such parameters with sufficiently high resolution. However, CCA needs a large number of independent pixels to derive them. As discussed by Bonaldi et al. (2006) a good compromise is to apply CCA to patches of about $1500\,\text{deg}^2$. We worked with patches of $(\Delta l, \Delta b) = (50°, 30°)$ on the Galactic plane, and increased Δl with increasing $|b|$ as necessary to roughly preserve the pixel number (and the patch area). We centered our patches at longitudes $l_c = \{0°, 40°, 80°, ...320°\}$ and latitudes $b_c = \{0°, \pm15°, \pm25°, \pm35°\}$.

The different sky patches intersect each other, but the overlap is small enough for them to be taken as independent of each other. In fact, the covariance matrices [eq. (8)] of adjacent patches are all substantially different from each other.

For any given input model CCA has then yielded the mixing matrix for each of the 63 patches. As discussed in the following subsection, the first use of these results was to give us some guidance in the selection of input models. In this analysis and throughout the whole paper we used the HEALPix tessellation scheme (Górski et al. 2005) [1].

---

[1] see http://healpix.jpl.nasa.gov

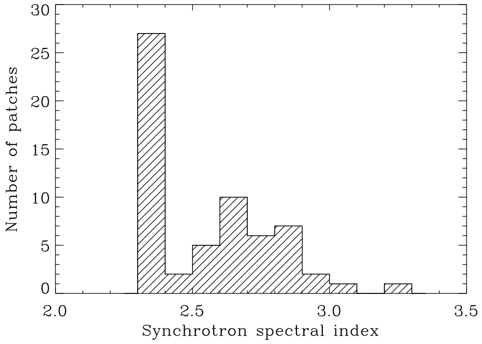

Figure 1. Distribution of the synchrotron spectral index β_s obtained by CCA for model **M1**.

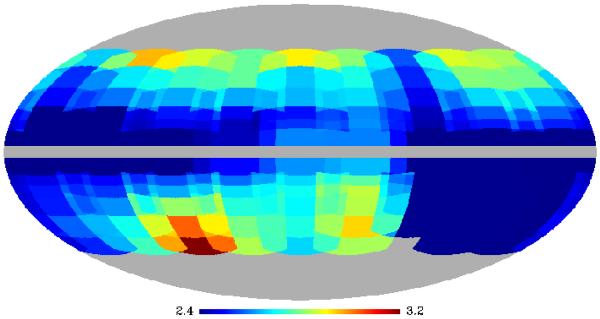

Figure 2. Map of the synchrotron spectral indices recovered by the CCA for model **M1**.

3.3.1 *The standard foreground model,* M1

We started our analysis adopting the most conservative model (which will be referred to as **M1**), containing the standard mixture of CMB, synchrotron, thermal dust and free-free. This model has only one free parameter, the synchrotron spectral index β_s. In fact, the spectral behaviour of the CMB and of the free-free emissions are known [eqs. (1) and (2)], and the thermal dust spectrum is only very poorly constrained by WMAP data, so that the results are very weakly dependent on the assumed dust temperature and emissivity index. We adopted the commonly used values $T_{\rm dust} = 18\,$K and $\beta_d = 1.67$ [eq. (4)].

The distribution of β_s obtained with CCA, shown in Fig. 1, presents two peaks. To determine position and width of the peaks we divided the distribution in two, $\beta_s \leqslant 2.4$ and $\beta_s > 2.4$, and fitted them with gaussian distributions. One peak is at $\beta_s \simeq 2.7$ and has a dispersion $\sigma \simeq 0.2$, which is roughly what is expected for synchrotron. The second one, at $\beta_s = 2.3852$, is extremely narrow $\sigma \simeq 0.0004$, hinting at a different component. We explicitly checked that this distribution is unaffected by different choices of the thermal dust parameters, within the observed ranges (§ 2). This immediately begs the question, what is this second flatter component.

In Fig. 2 we show the map of the recovered synchrotron spectral indices. Mean values are adopted in the regions where different patches overlap. The flattish component is mainly located at low latitudes, more than $\sim 40^\circ$ away from the Galactic center, and is not well correlated with the synchrotron template. In the next subsection we investigated different possible spectral shapes for this “anomalous” component.

3.4 Models for the “anomalous” component

As pointed out by many authors (e.g. de Oliveira-Costa et al. 2004; Watson et al. 2005), the spectral behaviour of the anomalous emission clearly differs from those of free-free and synchrotron at 10–15 GHz (where we don’t have all-sky maps), but is similar to them in the 20–40 GHz range. This means that any attempt to estimate simultaneously the spectral parameters of synchrotron and of the anomalous emission from WMAP data is liable to strong aliasing effects. We have therefore chosen to estimate the spectral parameters of the anomalous emission keeping β_s fixed, and repeating the analysis for several values of it in the range $2.8 \leqslant \beta_s \leqslant 3.1$. Specifically we ran CCA over all sky patches for $\beta_s = \{2.80, 2.86, 2.92, 2.98, 2.04, 3.10\}$.

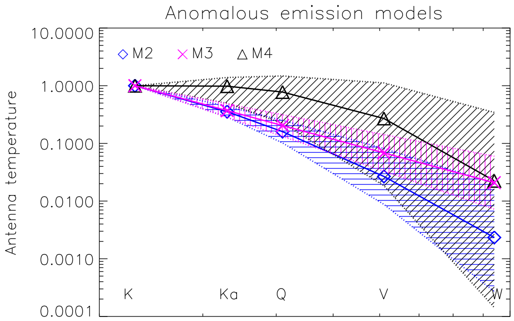

Figure 3. Frequency spectra of the anomalous emission for the models **M2**, **M3** and **M5**. The curves are normalized at the K band. For each model, the shaded area shows the range of values allowed for the esitmation, while the symbols refer to the central values.

As for the anomalous emission spectrum, we have investigated the models summarized in Table 2 with their free parameters, and described in the following. The proposed frequency scaling for the anomalous emission are also shown in Fig. 3.

3.4.1 *Model* M2

The results by de Oliveira-Costa et al. (2004), Watson et al. (2005), and Davies et al. (2006) suggest that the spectrum of the anomalous emission for $\nu > 20\,$GHz may be represented by a parabola in the $(\log\nu, \log S)$ plane with $\nu_{\rm max} = 20\,$GHz:

$$\log T_{\rm A,X}(\nu) = {\rm const} + \left(\frac{-m_{60}\log\nu_{\rm max}}{\log(\nu_{\rm max}/60\,{\rm GHz})} - 2\right)\log\nu + \\ -\frac{-m_{60}}{2\log(\nu_{\rm max}/60\,{\rm GHz})}(\log\nu)^2. \quad (10)$$

with ν in GHz. The free parameter, m_{60}, is the angular coefficient at the frequency of 60 GHz in the $(\log\nu, \log S)$ plane.

Running CCA for the above set of values for β_s we found that the mean values of m_{60} over the sky patches are in the range $3.8 \leqslant m_{60} \leqslant 4.5$, and correlate with β_s. The linear best fit relation, shown in Fig. 4, is:

$$m_{60} = (2.1101 \pm 0.0005)\beta_s - (2.073 \pm 0.002). \quad (11)$$

Table 2. Summary of the models

Model	investigated component	parametrization	free parameters and ranges
M1	Synchrotron	eq. (3)	$2.0 \leqslant \beta_s \leqslant 3.5$
M2	Anomalous emission	eq. (10); $\nu_{\rm max} = 20\,{\rm GHz}$	$1.0 \leqslant m_{60} \leqslant 5.0$
M3	Anomalous emission	$T_{\rm A,X}(\nu) \propto \nu^{-\beta_2}$	$2.0 \leqslant \beta_2 \leqslant 2.6$
M4	Anomalous emission	$T_{\rm A,X}(\nu) \propto [\nu^{\beta_x+1}]/[\exp(h\nu/kT_x)-1]$; $\beta_x = 2.4$	$0.2\,{\rm K} \leqslant T_x \leqslant 0.7\,{\rm K}$
M5	Thermal + Anomalous dust	eq. (14); $\nu_{\rm max} = 20\,{\rm GHz}$	$1.0 \leqslant m_{60} \leqslant 5.0,\ \ 0.1 \leqslant R_{60} \leqslant 2.0$

The corresponding spectral shape is compatible with the anomalous emission detected by Davies et al. (2006). In particular, our scaling between the K and Ka bands is almost the same they find, and the one between Ka and Q is very similar. Our model falls down more rapidly then theirs at higher frequencies, but is still inside their error bars.

3.4.2 Model **M3**

Alternatively, the anomalous emission might be interpreted as flat-spectrum synchrotron, possibly highly self absorbed, associated to strong magnetic fields local to star forming regions (and thus dust-correlated). To investigate this possibility we parameterize this component as a power law, with a spectral index β_2.

As before, we obtained the distribution of β_2 over the sky patches for each value of β_s. Such distribution turned out to be quite narrow (dispersion $\sigma = 0.003$) and independent of β_s. The mean value of the spectral index

$$\langle \beta_2 \rangle = 2.144 \tag{12}$$

turns out to be remarkably close to that of free-free, hinting at the possibility of aliasing effects. We will come back to this possibility in § 5.

3.4.3 Model **M4**

In this case we adopt for the anomalous component the spectrum used by Tegmark et al. (2000): it is a grey body, of the form of eq. (4), with temperature $T_x = 0.25\,{\rm K}$ and emissivity index $\beta_x = 2.4$. We checked that a simultaneous estimation of both β_x and T_x was not feasible, as the algorithm failed to converge. Then, we fixed $\beta_x = 2.4$ and allowed T_x to vary in the range $0.2\,{\rm K} \leqslant T_x \leqslant 0.7\,{\rm K}$.

As it can be seen looking at Fig. 3, **M2** and **M4** yield quite different frequency scalings. Infact, the latter has been proposed to fit typical Draine & Lazarian (1998) spinning dust models, but it is not suited to reproduce the results by Davies et al. (2006). Given the slope between the K and Ka bands, **M4** goes down more rapidly.

The results (Fig. 5) can be summarized as:

$$T_x = \begin{cases} 0.43 \pm 0.01\,{\rm K} & \text{if } \beta_s \leqslant 3.0 \\ 0.47 \pm 0.01\,{\rm K} & \text{if } \beta_s > 3.0. \end{cases} \tag{13}$$

The spectrum rises from K to Ka band, and slowly decreases going to higher frequencies. The slope between 60 and 94 GHz is consistent with what found for **M2**.

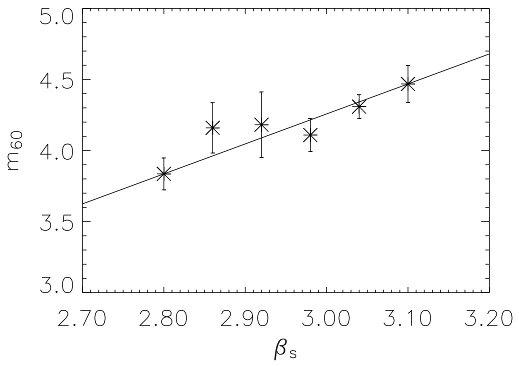

Figure 4. Mean estimated values of m_{60}, with their errors, vs assumed values of the synchrotron spectral index β_s (model **M2**).

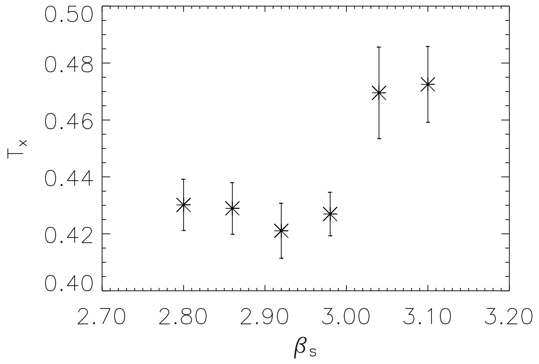

Figure 5. Mean estimated values of T_x, with their errors, vs assumed values of the synchrotron spectral index β_s (model **M4**).

3.4.4 Model **M5**

We tested the possibility that there is a perfect correlation between thermal dust and anomalous emission, so that they can be treated as a single component parameterized as:

$$T_{\rm A,dust+X}(\nu) \propto T_{\rm A,dust}(\nu) + R_{60} \cdot T_{\rm A,X}(\nu), \tag{14}$$

where $T_{\rm A,dust}$ is given by eq. (4) and $T_{\rm A,X}$ by eq. (10). The factor R_{60} quantifies the relative intensity of the two emissions at a frequency of 60 GHz. The free parameters of this model are R_{60} and m_{60}, whereas the other ones are fixed as in **M2**.

The recovered values of the parameters are shown in Fig. 6. The values of m_{60} are within the range found for model **M2**, which did not assume any correlation with thermal dust, but the correlation with β_s is now weaker. The linear best fit relations of m_{60} and R_{60} with β_s (solid lines in Fig. 6) are:

$$R_{60} = (-1.4 \pm 0.4)\beta_s + (4.4 \pm 1.2) \tag{15}$$

$$m_{60} = (1.3 \pm 0.3)\beta_s + (0.3 \pm 0.1). \tag{16}$$

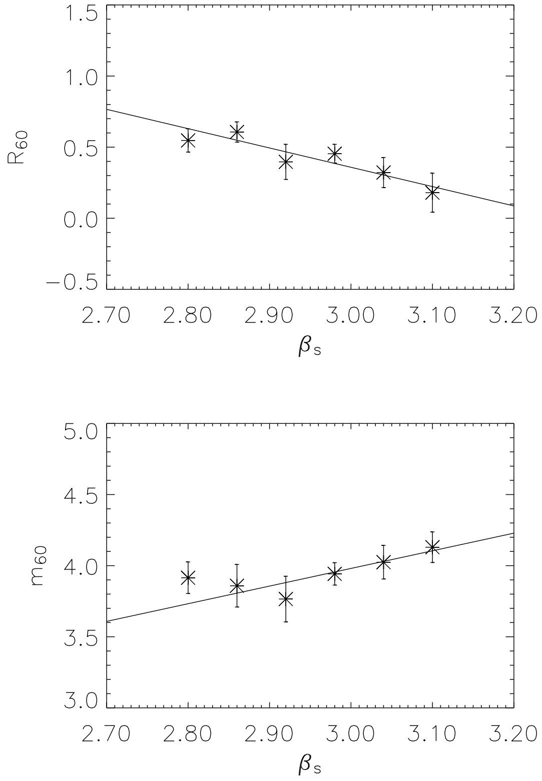

Figure 6. Mean estimated values of R_{60} and m_{60}, with their errors, vs assumed values of the synchrotron spectral index β_s (model **M5**).

This is again consistent with Davies et al. (2006), both for the slope m_{60} and the intensity ratio of the anomalous component respect to thermal dust R_{60}.

4 SOURCE RECONSTRUCTION WITH THE WF

Once the mixing matrices of the diffuse components in the WMAP data were estimated for the different models, we performed the source reconstruction with the harmonic Wiener Filtering. In the harmonic space the problem stated in eq. (5) simply becomes:

$$\mathbf{x}_{lm} = \mathbf{H}\mathbf{s}_{lm} + \mathbf{n}_{lm}, \tag{17}$$

where the vectors $\mathbf{x}_{lm}$, $\mathbf{s}_{lm}$, and $\mathbf{n}_{lm}$ contain the harmonic coefficients of channels, sources and instrumental noise, respectively. Using a linear approach to component separation, an estimate of the vector $\mathbf{s}_{lm}$, say $\hat{\mathbf{s}}_{lm}$, can be obtained as:

$$\hat{\mathbf{s}}_{lm} = \mathbf{W}^{(l)}_{\hat{H}}\mathbf{x}_{lm}, \tag{18}$$

where the reconstruction matrix $\mathbf{W}^{(l)}_{\hat{H}}$ depends on the estimate $\hat{\mathbf{H}}$ of the mixing matrix. In the case of Wiener Filtering, we have:

$$\mathbf{W}^{(l)}_{\hat{H}} = \mathbf{C_s}^{(l)}\hat{\mathbf{H}}^T[\hat{\mathbf{H}}\mathbf{C_s}^{(l)}\hat{\mathbf{H}}^T + \mathbf{C_n}^{(l)}]^{-1}, \tag{19}$$

where $\mathbf{C_s}$ and $\mathbf{C_n}$ are the source and the noise power spectra, respectively. If the source and the noise processes are uncorrelated, $\mathbf{C_s}$ and $\mathbf{C_n}$ are diagonal matrices. Even in this approximation, however, reconstructing the components with WF requires the knowledge of the diagonal elements $C_s^{(l)}(i) \equiv \mathbf{C_s}^{(l)}(i,i)$ and $C_n^{(l)}(i) \equiv \mathbf{C_n}^{(l)}(i,i)$. The latter can be easily modeled; in the case of uniform noise, we have:

$$C_n{}^{(l)}(i) = 4\pi\sigma_i^2/N_i, \tag{20}$$

where N_i is the number of pixels, and σ_i is the rms pixel noise. On the other hand, the power spectra of the components, $C_s^{(l)}$, are not, or only poorly, known a priori. A common approach (Hobson et al. 1998; Stolyarov et al. 2002) is to start from a rough estimate of the source power spectra $C_s^{(l)}(i)$ and get the reconstruction matrix through eq. (19). The latter allows us to get the estimated components through eq. (18). After the first reconstruction, we obtain $C_s^{(l)}(i)$ as the unbiased estimators of the power spectra of the reconstructed sources and we update $\mathbf{W}^{(l)}_{\hat{H}}$. The procedure is iterated until convergence on the power spectra is reached.

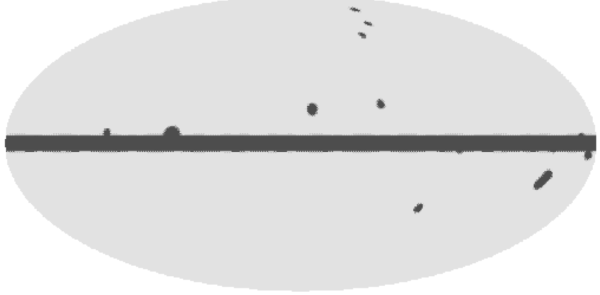

Figure 7. Apodized mask used to preprocess the input maps for WF. The minimum (dark grey) and maximum (light grey) values are 0 and 1 respectively.

To derive the initial power spectra, we performed a first, low-resolution, reconstruction through eq. (18) exploiting the reconstruction matrix:

$$\mathbf{W}^{(l)}_{\hat{H}} = (\hat{\mathbf{H}}^T(\mathbf{C_n}^{(l)})^{-1}\hat{\mathbf{H}})^{-1}\hat{\mathbf{H}}^T(\mathbf{C_n}^{(l)})^{-1}, \tag{21}$$

which corresponds to a maximum likelihood analysis. Note that in this case, besides the estimate of the mixing matrix $\hat{\mathbf{H}}$, recovered by CCA, only the prior knowledge of the noise power spectra $\mathbf{C_n}^{(l)}$ is required. We then use as initial $C_s^{(l)}(i)$ for the WF the power spectra of these reconstructed sources extrapolated to small scales assuming l^{-3} behaviour (Zavarise 2007). After convergence has been reached, dust, free-free and, if present, anomalous emission behave as l^{-2} between multipoles $\sim$ 10 and few hundreds, while synchrotron behaves as l^{-3}.

The approach just described uses a minimum number of priors: in practice, the components are identified only by their frequency scalings. The lack of prior covariance information certainly limits the quality of the reconstruction, but in this way we avoid biasing the results.

4.1 The WF data set

For the matrix inversion we used the WMAP K, Ka, Q, V, and W bands at their original resolution. Since we now work in the harmonic domain, a frequency-dependent beamwidth can be naturally accounted for. We assumed circularly symmetric gaussian beams with the FWHM values reported in Table 1. Even if this may not be a good approximation of the real beams, the effect of beam asymmetries is unlikely to be relevant on the relatively large angular scales we are considering here. The noise processes have been assumed to be uniform over the whole sky: to compute the noise levels we averaged the standard deviations of a set of simulated WMAP noise maps.

To take advantage of all the available information we complemented the WMAP data with the synchrotron, dust and free-free maps adopted for the mixing matrix estimation (see § 3). These maps have resolutions of $60'$, $5'$ and $60'$, respectively. We have allowed for the effect of variations of spectral indices of synchrotron and dust across the sky (while the inversion is done adopting everywhere the mean values obtained with CCA) by attributing to the corresponding maps uncertainties much larger than the measurements errors. In particular, we computed the standard deviation of each prior map outside the apodized mask of Fig. 7 and assumed a constant rms level of 20% for the 408 MHz synchrotron map and of 10% for the 850 GHz thermal dust map. The spread of spectral indices may induce even larger uncertainties, but we have checked that increasing the uncertainties by up to a factor of two has a negligible impact on the reconstruction of the CMB and a small effect on that of foregrounds. This problem does not affect the free-free for which we have adopted the nominal rms error of 7% (Dickinson et al. 2003).

Algorithms working in the spherical harmonics space require data maps defined over the whole sky. On the other hand, cutting out highly contaminated regions is generally necessary to recover the CMB map. But the spherical harmonic basis is no longer orthonormal over the cut sphere and correlations are introduced between harmonic coefficients at different (l, m) modes. As shown by Stolyarov et al. (2005), one way to overcome these problems is to consider the cut areas as an extreme case of anisotropic noise, where the noise becomes formally infinite. In this way we can work with all sky maps but the solution is not constrained in the omitted areas. Similar results are obtained, with less computational problems, by filling the masked areas with a noise realization at the nominal level for the considered channel (Stolyarov, private communication). To reduce edge effects the maps were weighted with the apodized mask shown in Fig. 7. This mask excludes the strip at $|b| < 3^\circ$, the LMC, the Cen A region, and regions of 1° radius centered on the brightest point sources. Obviously, all pixels which have been modified will be excluded from the analysis of the output maps.

4.2 Analysis

The CCA gives, for each model, the distribution of spectral parameters found in different sky patches. These distribution reflect (besides estimation errors) the spatial variability of the spectra. On the other hand, the harmonic Wiener Filtering is applied using a single mixing matrix over the full sky, i.e. assuming spatially uniform spectra. To investigate the effect of this simplification we generated a set of 30 mixing matrices for each model, drawing the spectral parameters at random from CCA distributions. For each matrix, we performed a full-sky source reconstruction up to $l = 300$.

In the cases of models **M2** and **M5**, we adopted, for β_s, the same distribution of **M1**, and derived the value of m_{60} or of R_{60} and m_{60} from eq. (11) or from eqs. (15) and (16), respectively. In the case of **M3**, we used the same uniform distribution for β_s and a Gaussian distribution for β_2. For **M4** we used the same uniform distribution for β_s and derived T_x according to eq (13).

A particular case is given by the standard foreground model, **M1**. The results obtained with CCA for this model indicate that, if no additional component is present, we cannot assume a uniform synchrotron spectral index all over the sky. Thus, generating a set of synchrotron spectral indices according to the distribution shown in Fig. 1 would not be meaningful. For this reason we used this model for reference, adopting for the synchrotron spectral index a uniform distribution in the range $2.8 \leqslant \beta_s \leqslant 3.1$.

5 RECONSTRUCTED COMPONENTS

In Fig. 8 we show the rms in the WMAP bands of the components reconstructed using each model. Only pixels outside the apodized mask of Fig. 7 have been taken into account.

On this plot, the CMB component shows tiny variations from one iteration to another (the shaded regions are too narrow to be visible) and also from a model to another, suggesting that the choice of the foreground model, among those considered here, has little influence on the CMB reconstruction. This will be better discussed in the next section, where we will focus our analysis on the CMB component. Variations are very small also for the reconstructed thermal dust and free-free components. This is due to the fixed frequency scaling and to the use of prior maps.

As expected, we have a substantial spread in the reconstructed synchrotron component, reflecting the wide range of synchrotron spectral indices used for the separation. This component is found to be generally sub-dominant compared to the free-free, except, possibly, in the K band, in agreement with the results by Hinshaw et al. (2006).

The results on the anomalous emission components are also quite stable. If we force this component to have a power-law spectrum (model **M3**) we find that it dominates over both synchrotron and free-free in all the WMAP channels. The anomalous emission for **M4** is found to dominate in the Ka, Q and V bands. Models **M2** and **M5** are consistent with each other, as the summed intensity of thermal dust and anomalous emission of model **M2** is close to that of the "total dust" emission of model **M5**. Moreover, they yield similar intensities for the remaining components. As previously stressed, models **M2** and **M5** yield results on the anomalous emission which are consistent with Davies et al. (2006).

5.1 Quality tests

Before proceeding with the analysis of the results we try to evaluate the goodness of the decomposition for each model. A standard method is to analyze the residual between the data and the reconstructed sources combined by means of the estimated mixing matrix:

$$\mathbf{r} \equiv \mathbf{x} - \hat{\mathbf{H}}\hat{\mathbf{s}}. \qquad (22)$$

The analysis of the residuals allows to check if, given a certain mixing matrix, our algorithm succeeds in finding a plausible decomposition of the data. In the case of a perfect reconstruction of the channels, **r** contains maps of pure noise, characterized by Gaussian statistics. Foreground residuals bring in non-Gaussianities. A visual inspection of the residuals show that some non-Gaussian features are present in the maps. In particular, we can discern traces of anisotropic noise, point sources and diffuse emissions, particularly at low Galactic latitudes. The first two features are related to effects that are not accounted for in our analysis. The latter is more interesting, because it also reflects our modeling and estimation errors.

Each model shows the worst contamination in the K band, even if models including the anomalous emission are generally more clean (see for example the comparison between **M1** and **M2**

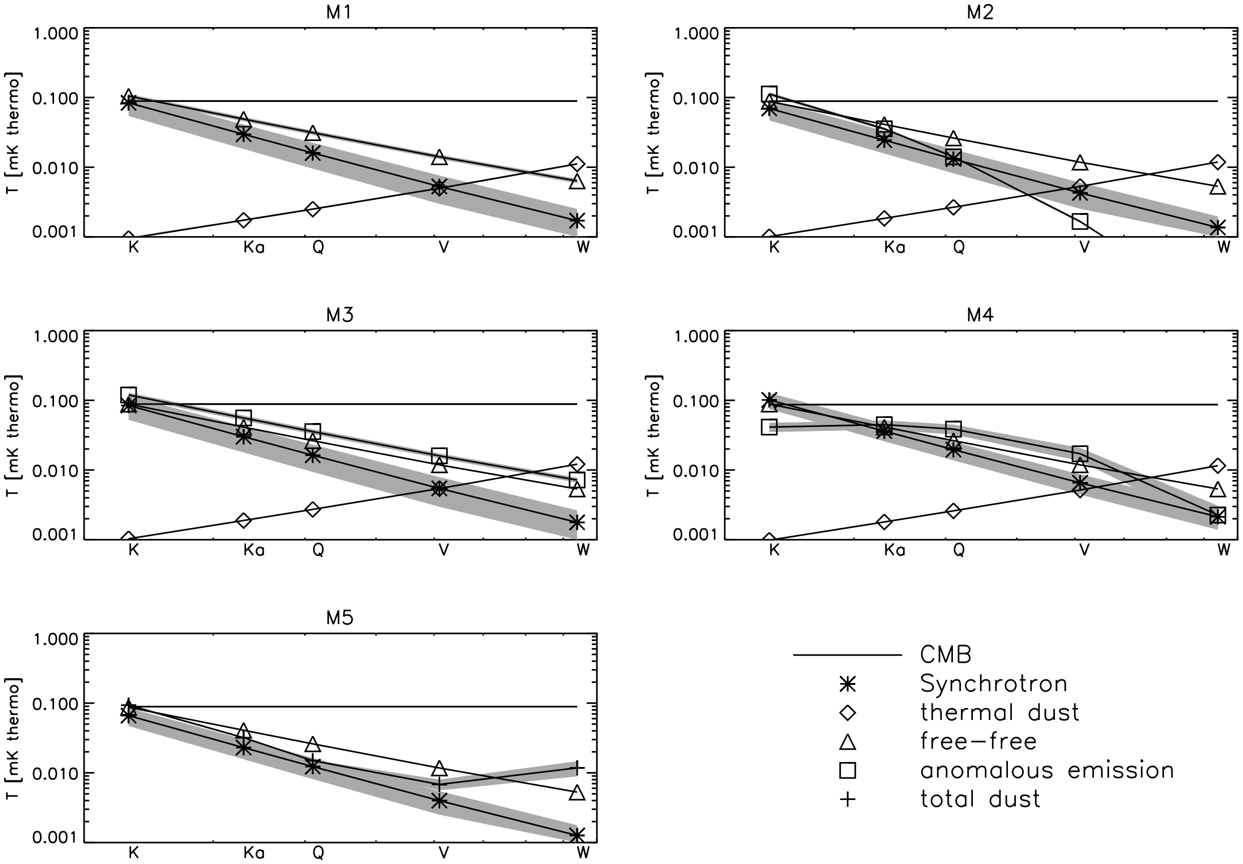

Figure 8. Frequency dependence of the rms fluctuations, in thermodynamic temperature, of the components reconstructed with each model. The shaded areas, visible only for components whose spectral parameters are allowed to vary, show the dispersion obtained from the 30 reconstructions per model, and the lines shows the mean spectra.

in Fig. 9). The "residual excess" at low latitudes then decreases at higher frequencies. The models **M1** and **M4** are generally worse; however this strongly depends on the synchrotron spectral index used for each separation.

More quantitative analyses of the residuals (power spectra, standardized moments of the distributions, etc.) mainly confirm these general findings, but turned out to be not very effective in discriminating among the models, as the results are comparable.

This means that, in our case, each model allows a satisfactory decomposition of the data, at least for a subset of synchrotron spectral indices. Neverthless, some of the models could still give uncorrect descriptions of the data. The analysis of the residuals, infact, is not informative on the reliability of the individual reconstructed components. For example, they may be affected by aliasing, which does not show up in the residuals. To investigate this possibility, we applied other quality tests directly based on the reconstructed components.

5.1.1 Correlation among the components

Independent observations have highlighted positive correlations of varying strength among synchrotron, free-free and dust emissions, ensuing from the physical processes producing them. Therefore, the reliability of the recovered components can be tested by investigating their mutual correlations. We have worked with pixels of area $0.84\,\mathrm{deg}^2$ (Nside = 64). We trimmed all pixels pre-processed through the apodized mask of Fig. 7 as well pixels within a radius of 1° around each point source listed in the WMAP three-year catalogue. We also excluded a region with a radius around 15° around the Gum Nebula, as in this region the separations are always very noisy. High Galactic latitude regions ($|b| > 50^\circ$), where foregrounds are weak and therefore recovered with low S/N ratios have also been excluded from the analysis. Around $3 \cdot 10^4$ pixels then remain.

For each model we have computed the correlation coefficients, r, among the recovered Galactic components for each of thirty separations. Whenever one of those coefficients was found to be negative, the corresponding separation was discarded. The percentages of discarded separations for each model are reported in Table 3. They are generally low ($\leqslant$ 10%), except in the case of **M3** (30%).

All the models including the anomalous component feature very strong positive correlations of it with thermal dust ($r \sim 0.8$), somewhat less strong but still highly significant positive correlations with synchrotron ($r \sim 0.6$), and weak positive correlations with free-free ($r \sim 0.25$).

For the large pixel number, $N \simeq 3 \times 10^4$, we are dealing with the correlation coefficient, r, for samples of uncorrelated quantities has a normal distribution with zero mean and $\sigma_r = 1/\sqrt{N}$. CMB and Galactic foregrounds are intrinsically uncorrelated; therefore, the presence of a statistically significant correlation among them

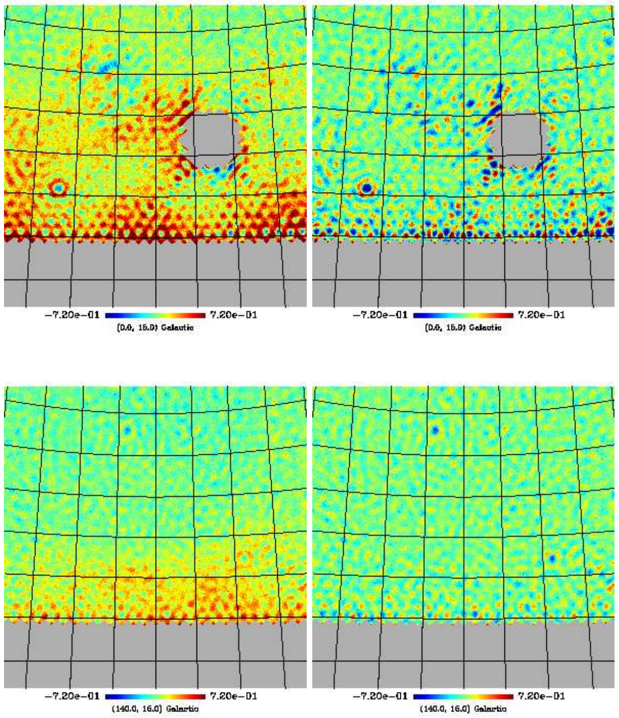

Figure 9. Residual at K band for model **M1** (left) and **M2** (righ) assuming $\beta_s \sim 3.$ in two regions of $\sim$ 40X40 degrees. Central coordinates of the patches are $l = 0^\circ$, $b = 15^\circ$ (up) and $l = 140^\circ$, $b = 15^\circ$ (down). Units are mK thermodynamic.

Table 3. Percentage of discarded separations because of negative correlation coefficients.

model	discarded separations
M1	0%
M2	6%
M3	30%
M4	10%
M5	3%

indicates a poor component separation. Thus, a good criterion to evaluate the quality of the separations is to compute the correlation coefficient between the reconstructed CMB and foreground maps. The latter have been obtained as the sum of the reconstructed components scaled to the Q and V bands. As in these bands the foreground contamination has a minimum, those correlations are expected to be low and, hopefully, not statistically significant. Once computed for each separation and each model, the correlation coefficients can be used as figures of merit to compare different models and, for a given model, to identify the best separations.

In Figure 10 we show the absolute values of the correlation coefficients as a function of the assumed synchrotron spectral index. The horizontal dashed line is the 3σ significance level.

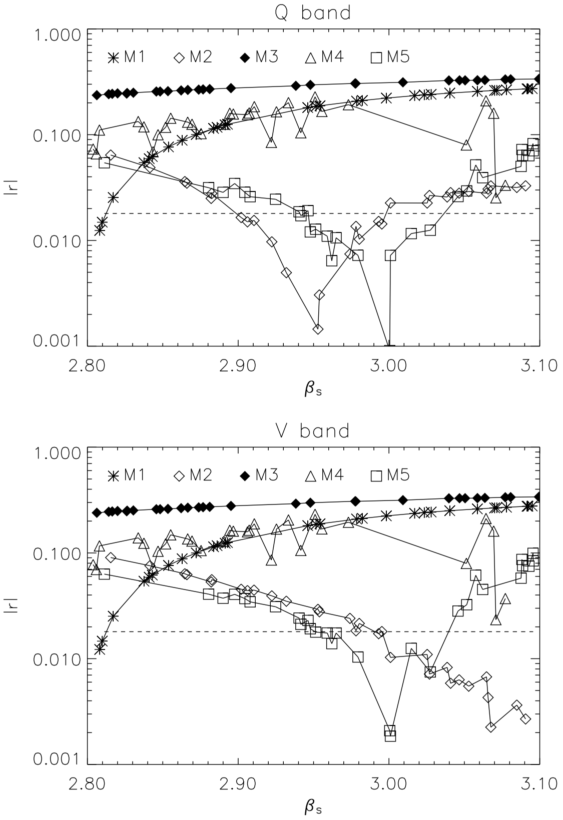

Figure 10. Absolute values of the correlation coefficient between the recovered CMB and the total foreground map for the Q (up) and V (down) bands as a function of the synchrotron spectral index. Values above dashed line correspond to correlations formally significant at $\geqslant 3\sigma$.

Model **M3** always features highly significant correlations ($r > 0.1$) between the CMB and the reconstructed foreground contribution in both bands, much stronger than found for the other models. This result, together with the high number of samples we had to discard due to aliasing effects, indicates that this model is not able to correctly describe the data. It was therefore discarded together with model **M4** which also yields values of $|r|$ always well above the 3σ limit, although somewhat below those found for **M3**.

In the case of models **M1**, **M2** and **M5**, the test shows that the correlations are not statistically significant for well defined ranges of the synchrotron spectral index. Model **M1** requires relatively low values of β_s, below that expected, in the WMAP frequency range, from the locally measured energy spectrum of relativistic electrons which would yield $\beta_s \simeq 3$ (Banday & Wolfendale 1990, 1991), as indeed found for models **M2** and **M5**.

We have built reference maps of each reconstructed component for each of the 3 surviving models by averaging those reconstructions with foreground–CMB correlations at less than 3σ level. For model **M2** we find somewhat different allowed ranges of β_s for the Q and the V bands, and we have kept the reconstructions in the union of the 2 ranges, i.e. with $2.9 \lesssim \beta_s \lesssim 3.1$. In Table 4 we list the correlation coefficients of the reference CMB map for each model with the foreground templates. The correlations computed with the minimal mask are formally statistically significant, indicating the presence of residual foreground contamination. The major contributions to the correlation coefficients come from regions close to the Galactic plane. If we adopt the WMAP kp2 mask, in place of our minimal mask, the correlation coefficients decrease, sometimes going close to or below the 3σ significance level, especially for free-free. In Table 5 we show the correlations of the reconstructed synchrotron, dust and free-free components with the

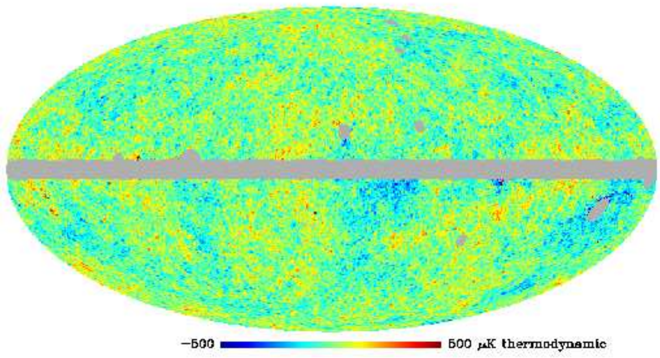

Figure 11. CMB map reconstructed with model **M2**.

Table 4. Correlation coefficients of the reconstructed CMB components with the foreground templates: minimal mask, (kp2 mask)

template	**M1**	**M2**	**M5**
thermal dust	0.027 (0.015)	0.029 (0.023)	0.025 (-0.023)
synchrotron	-0.054 (-0.046)	-0.016 (-0.012)	-0.015 (-0.010)
free-free	-0.035 (-0.021)	-0.035 (-0.0003)	-0.044 (-0.011)

Table 6. Correlation coefficients of the anomalous emission (**M2**) and of the total dust component (**M5**) with all the foreground templates.

template	**M2**	**M5**
thermal dust	0.823	0.883
synchrotron	0.664	0.711
free-free	0.294	0.221

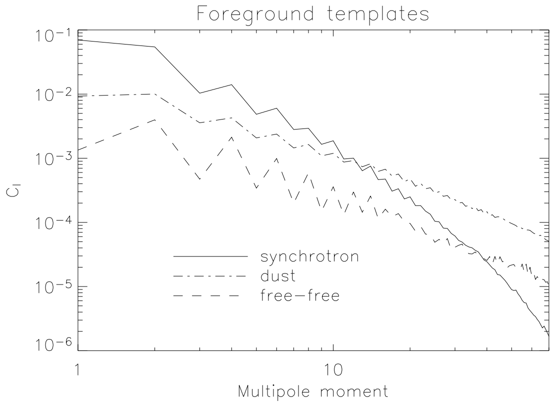

Figure 14. Full-sky power spectra of the foreground templates at low multipoles (arbitrary normalizations)

corresponding templates. The match between the prior and reconstructed maps is good but not perfect, as expected given the spatial variations of the spectral properties. Finally, Table 6 gives the correlation coefficients between the anomalous emission recovered with model **M2**, and the thermal dust plus anomalous emission recovered with model **M5** (which treats them as a single component with a complex spectrum), and the foreground templates. Interestingly, in the case of model **M2**, which does not impose a priori any correlation between thermal dust and anomalous emission, we find a tight, but not perfect, correlation among the 2 components. The anomalous emission also correlates strongly with synchrotron, and more weakly with free-free.

The final map of the anomalous component recovered with model **M2** is shown in Fig. 12, where the dust and synchrotron templates are also shown for comparison. Traces of imperfect component separation can be discerned by eye: negative imprints in correspondence of the Gum Nebula, of the Orion region and of the North Polar Spur, as well as several point-like sources. Nevertheless, this may be the first, albeit preliminary all-sky map of this component. The similarity with the thermal dust map is evident; we recall that no prior correlation of the anomalous emission with thermal dust was imposed. Differences with the spatial distribution of synchrotron are also clear: the anomalous emission is relatively stronger towards the outskirts of the Galaxy, where the first application of CCA found flat "synchrotron" spectral indices, and less prominent near the Galactic centre. In Fig. 13 we show a detail of the comparison between the thermal dust and anomalous emission maps recovered with **M2**. The area we show is the Region 6 of Davies et al. (2006), chosen to be dust dominated and poorly contaminated by free-free and synchrotron. In agreement with their results, the anomalous emission is detected in this region, and appears to be dust-correlated.

Table 5. Correlation coefficients of the synchrotron, thermal dust and free-free maps with the corresponding templates. We recall that for **M5** the dust component includes both the thermal and the anomalous contributions.

template	**M1**	**M2**	**M5**
thermal dust	0.966	0.967	0.883
synchrotron	0.865	0.858	0.851
free-free	0.957	0.984	0.984

6 THE CMB POWER SPECTRUM

The next question we wish to address is: to what extent do the different foreground models affect the estimates of the CMB power spectrum on large scales, where possible inconsistencies with predictions of the standard cosmological paradigm have been reported?

We will focus our analysis on $l \leqslant 70$, where the effect of fluctuations due to unresolved point sources, non included in our study, can be neglected. On large scales, however, the CMB maps reconstructed through matrix inversion of the WMAP data complemented with the three template foreground maps, keep trace of the spurious structure due to latter maps being mosaics of observations. This is clearly visible in Fig. 14 showing the power spectra of the templates at low multipoles. While for $l \gtrsim 10$ the power spectra are smooth, at lower multipoles there are conspicuous spikes, particularly for the free-free and the synchrotron. To avoid this problem, the CMB power spectrum for $l < 10$ was computed using only the WMAP data for the Wiener Filter reconstruction of the CMB, still using the same ranges of optimal spectral parameters for each model. For larger l's the inversion is carried out including the foreground templates. The error analysis, carried out as described in Bonaldi et al. (2006), confirms that this approach significantly decreases the errors on the power spectrum at low l's. The power

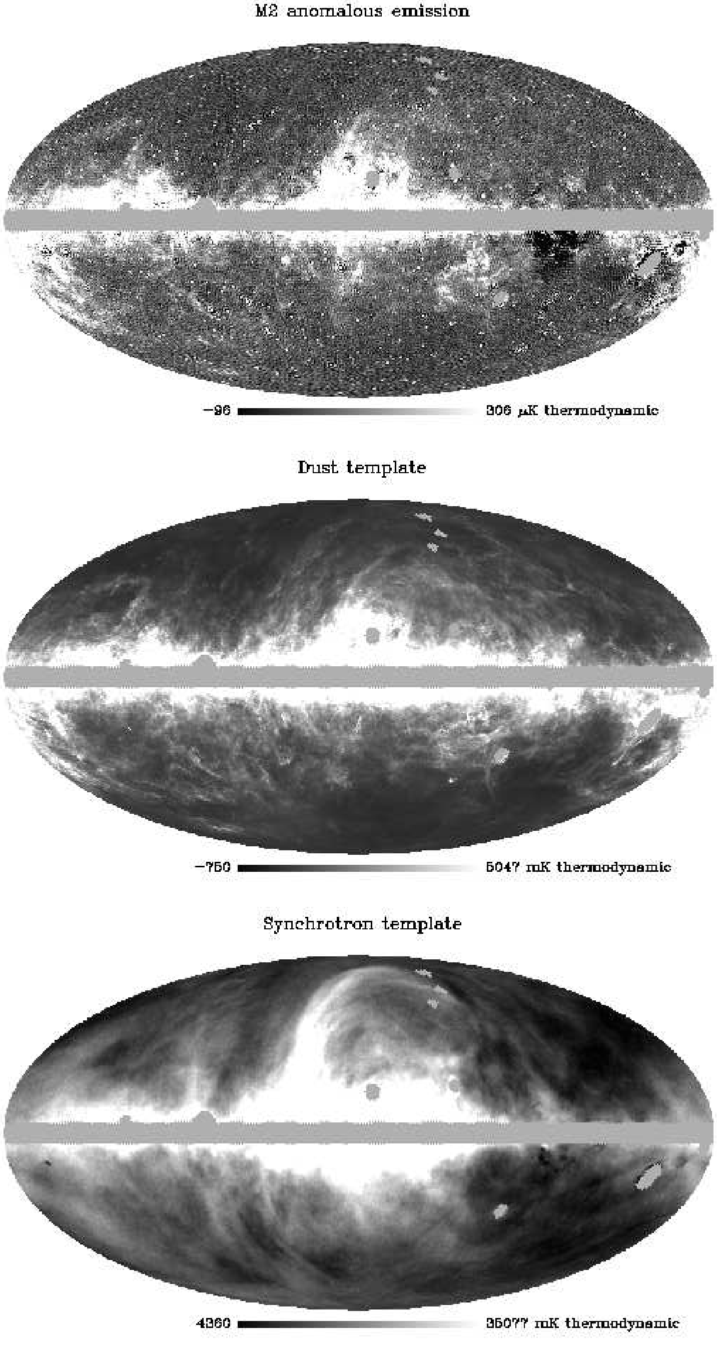

Figure 12. Map of the anomalous emission recovered with model **M2** in the K band compared with the dust (850 GHz) and the synchrotron (408 MHz) templates. Minimum and maximum value of the colour scales are given by the mean of the map ± its standard deviation.

spectra obtained with the two methods are very close to each other for $l \simeq 10$, so that they smoothly join and the choice of the boundary multipole needs not to be fine tuned.

In these calculations we used two sky masks. The first one (minimal mask) excludes all pixels having non unitary value in the apodized mask used to preprocess the data (Figure 7); the cut region amounts to $\sim 10\%$ of the sky. The second is the previous one multiplied by the WMAP kp2 mask; it excludes $\sim 20\%$ of the sky. The latter is less liable to residual foreground contamination, while the former is less liable to biases due to incomplete sky coverage. The power spectrum was binned with the same scheme adopted by the WMAP team and we applied the MASTER approach (Hivon et al. 2002) to get an unbiased estimate.

The results for each model are shown in Fig. 15, where we have plotted the power spectra computed with the minimal mask for $l \leqslant 8$, those computed with the other mask for higher multipoles. Again the results are weakly dependent on the choice of the mask, but the minimal mask yields smaller oscillations at low l's. We find generally a good agreement with the WMAP power spectrum, shown by the solid line. There are however significant

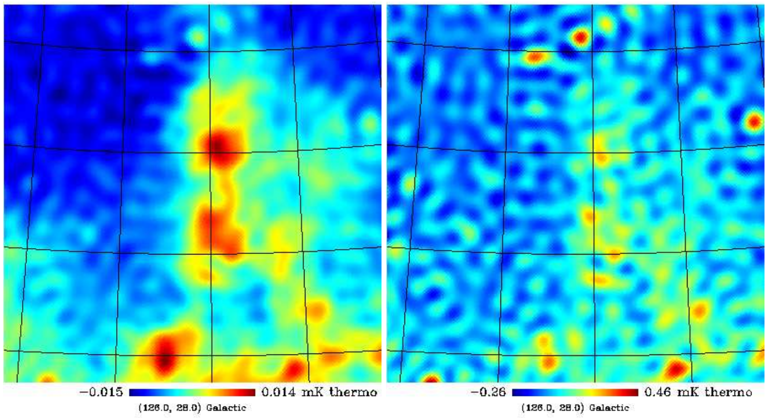

Figure 13. Recovered dust (left) and anomalous emission (righ) in Region 6 of Davies et al.(2006). Fluxes (mK thermodynamic) are at W and K band respectively.

differences among the various models at the lowest multipoles, especially evident for $l = 2$. Regardless to which are the actual models we are exploiting, this result shows that the hypotheses on the Galactic components made to perform component separation can be painful for the CMB power spectrum at larger scales. Thus, big error bars are required to take into account for possible biases at these multipoles. As an estimate of uncertainties associated to foreground modeling, we can take the spread of our three CMB power spectra.

In the upper panel of Fig. 16 we compare our results with the WMAP three year power spectrum and with the best fit ΛCDM model based on WMAP data only (Spergel et al. 2006). The mean quadrupole moment coming out from our analysis is higher than the WMAP estimate, and the difference with the prediction of the ΛCDM model is within the uncertainty due to cosmic variance. The spread of estimates of the quadrupole moment from different models is of about $\pm 200 \mu\mathrm{K}^2$.

Summing in quadrature the cosmic variance and the modeling errors, we find no large scale power spectrum "anomalies" significant at $\geqslant 1.5\sigma$, except for the excess power at $l \simeq 40$, which is significant at $\simeq 4\sigma$. On the other hand, as show by Fig. 17, the North-South asymmetry at $l \lesssim 20$ stands, independently of the adopted foreground model. Those power spectra, computed for each model for the North and for the South hemisphere separately, were obtained as previously described, except for the different binning scheme adopted.

7 CONCLUSIONS

We have performed the component separation on WMAP maps exploiting CCA technique to estimate the mixing matrix directly from the WMAP data, taking also into account the complementary information from the Haslam et al. (1982) 408 GHz map, from the extinction corrected Hα map (Dickinson et al. 2003), and from the combined COBE/IRAS thermal dust maps (Finkbeiner et al. 1999). The Hα map is exploited also to subtract the free-free contribution, which is substantial in some regions of the Galactic plane, from the Haslam et al. (1982) map, thus obtaining a pure synchrotron template.

The CCA is particularly useful to deal with possible additional

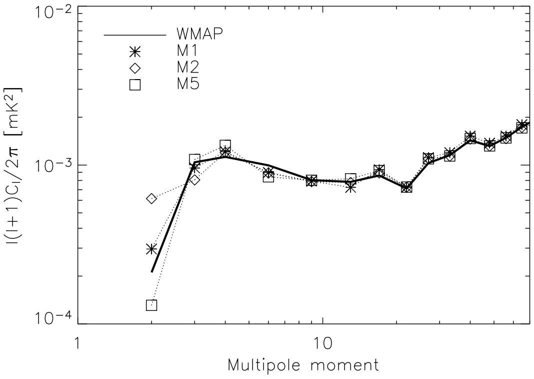

Figure 15. Binned CMB power spectra obtained from all models compared to the WMAP three-year power spectrum

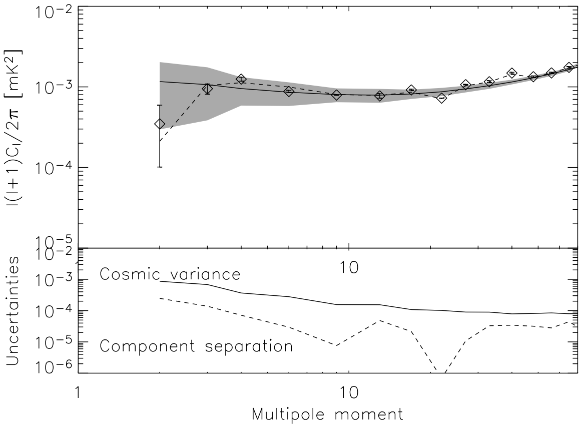

Figure 16. Upper panel: best fit ΛCDM model(smooth solid line) compared to the WMAP CMB power spectrum (dashed line) and to the mean final power spectrum resulting from our analysis (open diamonds; the error bars show the spread of results for different models). The shaded area shows the cosmic variance. Lower panel: uncertainties associated to foreground modeling (dotted line) compared to the cosmic variance (solid line).

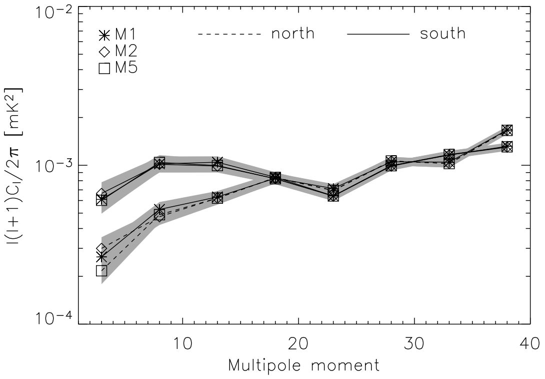

Figure 17. North-south asymmetry. The bins adopted have central multipoles $l = \{3, 8, 13, 18, 23, 28, 33, 38\}$ and equal width $\Delta l = 5$

.

foreground components, for which little or no prior information exists. An application assuming that only the canonical Galactic emissions (synchrotron, free-free, and thermal dust) are present highlights the widespread presence of a spectrally flat "synchrotron" component (Fig. 1), largely uncorrelated with the synchrotron template (compare Fig. 2 with the synchrotron template in Fig. 12), suggesting that an additional component is required.

We have then tested various spectral shapes for such component, namely a power law (model **M3**) as expected if it is a flat synchrotron emission due to enhanced magnetic fields in dusty star-forming regions, or a parabola in the $\log S$–$\log \nu$ plane (model **M2**), or a grey body, as proposed by Tegmark et al. (2000; model **M4**). In all these cases, the spatial distribution of this component was left totally unconstrained, but we have also tested the possibility that it is distributed exactly as thermal dust (model **M5**).

The CMB maps yielded by models **M3** and **M4** turned out to be substantially correlated with foreground maps, indicating a unacceptably large residual contamination. These models were therefore discarded. Conversely, in the case of models **M2** and **M5** the correlations were found to be not statistically significant for values of the synchrotron spectral index, $\beta_s \simeq 3$, close to the expectations from the slope of the locally measured energy spectrum of relativistic electrons (Banday & Wolfendale 1990, 1991). The data do not allow us to clearly discriminate among these models; however, some interesting indications emerge:

- The additional component turns out to be always tightly correlated with thermal dust although, if its spatial distribution is unconstrained, the correlation is not perfect (correlation coefficient $r \simeq 0.8$). This reminds us the suggestion by Davies et al. (2006) that, if this component is due to spinning dust, it should be better correlated with the small grains dominating the mid-IR emission than with the big grains dominating at far-IR to sub-mm wavelengths. The map of this component yielded by model **M2** could then constitute its first, albeit preliminary all sky map.
- The additional component is well correlated with synchrotron (correlation coefficient $r \simeq 0.6$) and more weakly correlated with the free-free, although the free-free is strongly correlated with thermal dust (correlation coefficient $r = 0.4 - 0.6$). The synchrotron is also well correlated with thermal dust (correlation coefficient $r = 0.7 - 0.8$), and more weakly with the free-free (correlation coefficient $r \simeq 0.2$).
- If only the standard Galactic emissions (synchrotron, free-free and thermal dust) are taken into account, we obtain acceptable separations adopting a flat synchrotron spectral index ($\beta_s \sim 2.8$). However, this value of β_s is not supported by the CCA analysis and is flatter than expected in the WMAP frequency range (Banday & Wolfendale 1990, 1991).
- The CMB maps we obtain have low foreground contamination even at low Galactic latitude, as demonstrated by the correlation with the foreground templates. The inclusion of the anomalous emission decreases the synchrotron contamination.

We have used the MASTER approach (Hivon et al. 2002) to obtain unbiased estimates of the CMB power spectrum up to $l = 70$ from maps reconstructed on the basis of each foreground model. The results are generally consistent with the WMAP ones, although we find a substantial spread of values for the quadrupole moment. For model **M2** the quadrupole moment is fully consistent with the expectation from the "concordance" cosmological model. The spread of power spectrum estimates gives us a measure of uncertainties associated to foreground modeling. Such uncertainties are smaller than the cosmic variance, but nevertheless significant, for $l \lesssim 30$, and approach it for larger l's. Combining the cosmic variance with the modeling errors, we find that the quadrupole amplitude is less than 1σ below that expected from the standard ΛCDM model. Also the other reported deviations from model predictions are found not to be statistically significant, except for the excess power at $l \simeq 40$. On the other hand, the North-South asymmetry is found to be unrelated to foreground models. The derived CMB power spectra are remarkably stable: even those yielded by the discarded models are within the range of Fig. 16.

REFERENCES

Banday A. J., Wolfendale A. W., 1990, MNRAS, 245, 182
Banday A. J., Wolfendale A. W., 1991, MNRAS, 248, 705
Bedini L., Herranz D., Salerno E., Baccigalupi C., Kuruoğlu E. E., Tonazzini A., 2005, EURASIP Journal on Applied Signal Processing, 2005, 2400
Bennett C. L., et al., 2003, VizieR Online Data Catalog, 214, 80097
Bonaldi A., Bedini L., Salerno E., Baccigalupi C., de Zotti G., 2006, MNRAS, 373, 271
Davies R. D., Dickinson C., Banday A. J., Jaffe T. R., Górski K. M., Davis R. J., 2006, MNRAS, 370, 1125
de Oliveira-Costa A., Kogut A., Devlin M. J., Netterfield C. B., Page L. A., Wollack E. J., 1997, ApJ, 482, L17
de Oliveira-Costa A., Tegmark M., Davies R. D., Gutiérrez C. M., Lasenby A. N., Rebolo R., Watson R. A., 2004, ApJ, 606, L89
de Oliveira-Costa A., Tegmark M., Finkbeiner D. P., Davies R. D., Gutierrez C. M., Haffner L. M., Jones A. W., Lasenby A. N., Rebolo R., Reynolds R. J., Tufte S. L., Watson R. A., 2002, ApJ, 567, 363
de Oliveira-Costa A., Tegmark M., Gutierrez C. M., Jones A. W., Davies R. D., Lasenby A. N., Rebolo R., Watson R. A., 1999, ApJ, 527, L9
de Oliveira-Costa A., Tegmark M., Page L. A., Boughn S. P., 1998, ApJ, 509, L9
Dickinson C., Davies R. D., Davis R. J., 2003, MNRAS, 341, 369
Draine B. T., Lazarian A., 1998, ApJ, 508, 157
Dupac X., Bernard J.-P., Boudet N., Giard M., Lamarre J.-M., Mény C., Pajot F., Ristorcelli I., 2003, in Combes F., Barret D., Contini T., Pagani L., eds, SF2A-2003: Semaine de

l'Astrophysique Francaise Inverse temperature dependence of the dust submillimeter spectral index. pp 207–+
Finkbeiner D. P., 2004, ApJ, 614, 186
Finkbeiner D. P., Davis M., Schlegel D. J., 1999, ApJ, 524, 867
Górski K. M., Hivon E., Banday A. J., Wandelt B. D., Hansen F. K., Reinecke M., Bartelmann M., 2005, ApJ, 622, 759
Haslam C. G. T., Salter C. J., Stoffel H., Wilson W. E., 1982, A&AS, 47, 1
Hinshaw G., et al., 2006, submitted to ApJ(astro-ph/0603451)
Hivon E., Górski K. M., Netterfield C. B., Crill B. P., Prunet S., Hansen F., 2002, ApJ, 567, 2
Hobson M. P., Jones A. W., Lasenby A. N., Bouchet F. R., 1998, MNRAS, 300, 1
Lagache G., 2003, A&A, 405, 813
Mukherjee P., Coble K., Dragovan M., Ganga K., Kovac J., Ratra B., Souradeep T., 2003, ApJ, 592, 692
Mukherjee P., Jones A. W., Kneissl R., Lasenby A. N., 2001, MNRAS, 320, 224
O'Dwyer I. J., 2005, PhD thesis, University of Illinois at Urbana-Champaign
O'Dwyer I. J., Eriksen H. K., Wandelt B. D., Jewell J. B., Larson D. L., Górski K. M., Banday A. J., Levin S., Lilje P. B., 2004, ApJ, 617, L99
Page L., et al., 2006, submitted to ApJ(astro-ph/0603450)
Paladini R., De Zotti G., Davies R. D., Giard M., 2005, MNRAS, 360, 1545
Rybicki G. B., Lightman A. P., 1979, Astronomy Quarterly, 3, 199
Schlegel D. J., Finkbeiner D. P., Davis M., 1998, ApJ, 500, 525
Slosar A., Seljak U., 2004, Physical Review D, 70, 083002
Slosar A., Seljak U., Makarov A., 2004, Physical Review D, 69, 123003
Spergel D. N., et al., 2006, submitted to ApJ(astro-ph/0603449)
Stolyarov V., Hobson M. P., Ashdown M. A. J., Lasenby A. N., 2002, MNRAS, 336, 97
Stolyarov V., Hobson M. P., Lasenby A. N., Barreiro R. B., 2005, MNRAS, 357, 145
Tegmark M., Eisenstein D. J., Hu W., de Oliveira-Costa A., 2000, ApJ, 530, 133
Watson R. A., Rebolo R., Rubiño-Martín J. A., Hildebrandt S., Gutiérrez C. M., Fernández-Cerezo S., Hoyland R. J., Battistelli E. S., 2005, ApJ, 624, L89
Zavarise P., 2007, Master's thesis, University of Padova, Italy